Correlation between the exchange bias effect and antisite disorder in $Sr_{2-x}La_xCoNbO_6$ ($x = 0, 0.2$)

Ajay Kumar,[1] B. Schwarz [●],[2] and R. S. Dhaka [●][1,*]

[1]*Department of Physics, Indian Institute of Technology Delhi, Hauz Khas, New Delhi-110016, India*
[2]*Institute for Applied Materials (IAM), Karlsruhe Institute of Technology (KIT), 76344, Eggenstein-Leopoldshafen, Germany*

We unravel the effect of La substitution and hence antisite disorders on the exchange bias (EB) mechanism in $Sr_{2-x}La_xCoNbO_6$ ($x = 0, 0.2$) double-perovskite samples using the detailed analysis of the field cooled magnetization isotherms (M-H) and training effect. The field dependence of the freezing temperature deviates from both Gabay-Toulouse and de Almeida-Thouless lines and the analysis suggests that the $x = 0$ sample follows a different universality class with moderate anisotropy in the frozen spins. Interestingly, we find that the EB effect is significantly suppressed in the $x = 0.2$ sample due to increase [decrease] in the size of ferromagnetic (FM) [cluster glass (CG)] domain, which reduces the effective disordered interface responsible for the EB. The changes in fraction of FM, antiferromagnetic, and CG-like interactions with the La substitution and applied magnetic field are found to be crucial in governing the EB effect in these samples. Furthermore, the training effect measurements show the unequal shift in the left and right branches of the M-H loops and their different evolution with the field cycles (n). The analysis reveals that the rotatable spins relax approximately one order of magnitude faster than the frozen spins at the disordered interface. We find a possible correlation between the observed EB effect and the antisite disorders in these samples.

I. INTRODUCTION

The exchange bias (EB) effect arises from the unidirectional magnetic anisotropy resulting from the exchange interactions at the ferromagnetic–antiferromagnetic (FM–AFM) interface and is manifested by a horizontal and/or vertical shift in the M-H loop, recorded after cooling the sample in the applied magnetic field below the AFM transition temperature (T_N) [1,2]. In addition to the FM–AFM interface, the EB effect has also been observed at the FM–ferrimagnetic (FiM), AFM–FiM, FM–spin glass (SG), AFM–SG, and FiM-SG disordered interfaces due to frustration in the spins [3–7]. The materials showing the EB effect are being extensively studied due to their wide range of technological applications in spin valves [8], hard magnets [9], magnetic random access memories (MRAM) [10–12], and various spintronic devices [13–15]. The degree and direction of the EB effect are governed by the nature of the exchange interactions at the interface. Thus, a precise understanding and control on the various exchange parameters at the magnetically disordered interfaces are necessary to engineer the suitable candidates for device applications. Also, the EB effect involving the spin glassy phase(s) exhibits the more complex phenomena due to the presence of the intrinsically frozen spins and is

crucial for their fundamental and technological aspects [5–7,16]. For example, the cluster glass (CG) behavior was recently found to govern the giant exchange bias of ≈ 9.6 kOe in $SrLaFe_{0.5}Mn_{0.25}Co_{0.25}O_4$ sample for a cooling field of 50 kOe [7].

In this context, the Co–based perovskite oxides have gained huge attention due to various possible valence and spin states of Co in the octahedral environment, resulting in several competing magnetic interactions and hence peculiar magnetic ground states such as spin glass, cluster glass, spin liquid, spin ice, Griffiths phase, etc. [17–22]. These low-temperature frustrated magnetic states can be systematically manipulated by the external perturbations such as temperature, mechanical pressure, chemical pressure (doping), magnetic field, etc. [17,18,20]. Furthermore, the double-perovskite (DP) oxides having general formula $A_2BB'O_6$ (A is the rare-earth or alkali earth metals, and B and B′ are the transition metals) can crystallize either in the ordered configuration with the alternating BO_6 and $B'O_6$ octahedra at the corners, or in the disordered state with two consecutive BO_6 or $B'O_6$ octahedra. These configurations give rise to B-O-B′-O-B and B′-O-B-O-B′, and B-O-B and B′-O-B′ exchange interactions, respectively [23]. Therefore, the fraction of various exchange interactions in DPs can be precisely controlled by varying the structural ordering, which is mainly governed by the ionic and valence mismatch between the two B-site cations [23–28], as well as strain [29,30]. For instance, the antisite (B-site) disorders in $LaSrCoFeO_6$ give rise to the Co^{3+}-Co^{3+}, Co^{3+}-Co^{4+}, Co^{4+}-Co^{4+}, Fe^{3+}-Fe^{3+}, Fe^{3+}-Fe^{4+}, and Fe^{4+}-Fe^{4+} AFM exchange interactions, whereas the ordered domains exhibit Co^{3+}-Fe^{4+} and Co^{4+}-Fe^{3+} FM couplings [6]. These competing AFM-FM interactions result in the low-temperature SG

*rsdhaka@physics.iitd.ac.in

behavior and a large EB effect in this sample [6]. The spin-glass-like phase is reported to play a key role in governing the largest zero-field-cooled EB effect in $La_{1.5}A_{0.5}CoMnO_6$ (A = Ba, Ca, Sr) samples [31,32]. In addition, the antisite disorder induced glassy behavior and the EB effect were observed at the interface of the long-range FM or AFM ordered and glassy phases in Gd_2CoRuO_6 [27], Sr_2FeCoO_6 [33], Pr_2CoMnO_6 [34], $La_{1.5}Ca_{0.5}CoIrO_6$ [35], $La_{2-x}Sr_xCoMnO_6$ [36], Eu_2CoMnO_6 [37], etc.

The Sr_2CoNbO_6 is one of the best prototype for understanding the complex EB mechanism in the magnetically disordered DPs due to the presence of only one magnetic cation (as Nb^{5+}; $4d^0$ remains nonmagnetic) and delicate antisite disorders in this sample [26,38]. The moderate ionic and valence mismatch between the Co^{3+} and Nb^{5+} ions [23,39] give rise to a site ordering with a correlation length of <100 Å [38], but a macroscopically disordered crystal structure [26,38,40], resulting in the intriguing magnetic ground state of Sr_2CoNbO_6 [26,38,41]. Also, the low-temperature spin-glass dynamics was reported in the Sr_2CoNbO_6 based on the memory effect and ac susceptibility data [38]. These investigations were further supported by our recent thermoremanent magnetization (TRM) and the aging effect measurements performed on $Sr_{2-x}La_xCoNbO_6$ samples [41]. The detailed analysis of the ac susceptibility data indicate the cluster glass like behavior in the $Sr_{2-x}La_xCoNbO_6$ samples for $x \leqslant 0.4$, where the size of the glassy cluster, intercluster interactions, and spin-spin correlation strength within the cluster decreases with the La substitution [41]. Moreover, the x-ray diffraction (XRD), neutron diffraction (ND), and extended x-ray absorption fine structure (EXAFS) measurements indicate a monotonic enhancement in the B-site ordering with La substitution in $Sr_{2-x}La_xCoNbO_6$, which is found to play an important role in governing the low-temperature complex spin dynamics in these samples [26,40,42]. Note that the antisite disorders are known to favor the EB effect in several DP oxides; however, unlike the present case, the precise control of these disorders is a major challenge. Therefore, it is vital to explore the possibility of the EB effect resulting from several competing magnetic interactions in these samples and their direct correlation with the degree of B-site ordering. Such a correlation can lead to a much deeper insight of the complex EB mechanism in the DPs and will be useful in engineering the potential candidates for the technological applications, as the B-site disorders can be precisely controlled with the La concentration in these samples.

In this paper, we present the effect of antisite disorders on the frozen spins and hence EB phenomena in $Sr_{2-x}La_xCoNbO_6$ (x = 0, 0.2) samples, which are having significant antisite disorders and cluster-glass nature of magnetic phase [26,41]. In the first section, we investigate the field dependence of the irreversibility temperature T_{irr} in the zero-field-cooled (ZFC) and field-cooled (FC) magnetic susceptibility curves for the x = 0 sample, which shows deviation from both Gabay–Toulouse (GT) and de Almeida–Thouless (AT) lines, and the analysis suggests the moderate exchange anisotropy in this sample. In the next section, we present the field dependence of the EB effect in the x = 0 and 0.2 samples and find that the EB parameters increase with the cooling field H_{CF} up to a certain value and then decreases with further

increases in the H_{CF} for both the samples. More importantly, the La substitution significantly reduces the EB effect due to enhancement in the size of the FM domains, which reduces the effective disordered interface. Then, we performed the training effect measurements on both the samples and use various models to understand the low-temperature complex spin dynamics. We observe the asymmetric training effect in both the samples and a more stable EB mechanism in case of the x = 0.2 sample. In the last section, we discuss the possible origins and evolution of the EB effect and their correlation with the antisite disorders in these samples.

II. EXPERIMENT

The polycrystalline samples of $Sr_{2-x}La_xCoNbO_6$ (x = 0 and 0.2) were synthesized by usual solid-state reaction route. The detailed synthesis process and physical properties can be found in our recent papers [26,40–42]. The magnetization measurements were performed using the Physical Property Measurement System (PPMS) from Quantum Design, USA. The details of the protocols for different measurements are provided along with their respective discussion in the next section.

III. RESULTS AND DISCUSSION

A. Field dependence of blocking temperature

In Figs. 1(a)–1(f), we show the zero-field-cooled (ZFC) and field-cooled (FC) magnetic susceptibility ($\chi = M/H$) curves of the x = 0 sample, recorded at different magnetic fields to probe the low-temperature complex spin dynamics [26,41]. A clear bifurcation in the two curves is observed below 15 K at 100 Oe, which shifts to the lower temperature with increase in the applied magnetic field, as indicated by the dashed arrow in Fig. 1. This is the typical signature of the magnetically disordered systems with glassy ground state, where the higher applied magnetic field align even the blocked spins at the low temperature [24,43–46]. Here, it is interesting to note that the ZFC curves show a decreasing tendency below a certain temperature T_{irr} and then increases with further decrease in the temperature for the low applied fields [see Figs. 1(a)–1(d) up to 20 kOe], unlike conventional glassy systems, where these curves decrease monotonically on lowering the temperature [24,47]. However, this upturn in the ZFC curves below 5 K gradually becomes downturn at the higher applied magnetic fields $\geqslant$20 kOe [see Figs. 1(e) and 1(f)], which rules out the paramagnetic impurities as the origin of this low-temperature upturn for $H \leqslant 20$ kOe. The similar temperature and field dependence of the ZFC behavior is also reported in the several other disordered compounds [48–50]. In the present case, an enhancement in the fraction of FM component and hence weakly saturating behavior of the M-H curves (presented in next section) results in this low-temperature downturn in the ZFC curves at the higher magnetic fields. This effect is more clearly observed in the exchange bias effect measurements performed at the higher cooling fields, discussed in detail below. Moreover, the magnetic susceptibility χ monotonically decreases with increase in the field even up to 30 K [see inset of Fig. 1(f) for the field dependence of χ at 30 K], which indicates the presence of
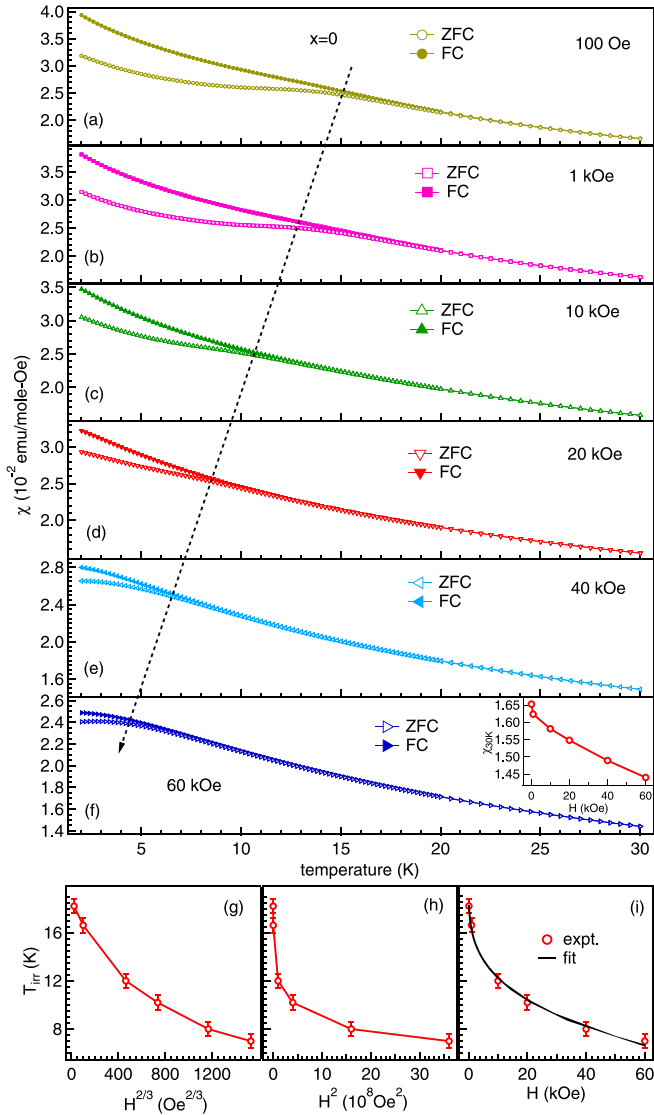
FIG. 1. (a)–(f) The ZFC and FC magnetic susceptibility curves recorded at different magnetic fields, H for the $x = 0$ sample, where an arrow represents the shift in the irreversibility temperature T_{irr}. Inset in panel (f) shows the field dependence of the magnetic susceptibility at 30 K. The variation of T_{irr} with (g) $H^{2/3}$, (h) H^2, and (i) H (see text for more details). The black solid line in panel (i) represents the best fit using Eq. (1).

short-range magnetic correlation in the sample well above the blocking temperature.

Furthermore, we analyze the magnetic field dependence of the irreversibility temperature in the ZFC–FC curves (T_{irr}) using the following power law [48,51,52]:

$$T_{\text{irr}}(H) = T_{\text{irr}}(0)[1 - AH^p], \tag{1}$$

where $T_{\text{irr}}(0)$ is the irreversibility temperature in the zero-field regime, A is a constant which is the measure of the anisotropy in the system, and the value of power exponent p defines the nature of the magnetic interactions. For the highly anisotropic Ising spins, the value of p is 2/3, which gives de Almeida–Thouless (A-T) line, whereas $p = 2$ in the weak anisotropy regime corresponds to the Gabay–Toulouse

(G-T) line [44,53]. To check this, we plot the T_{irr} as a function of $H^{2/3}$ and H^2 in Figs. 1(g) and 1(h), respectively. Interestingly, we observe a clear deviation from the linearity in both the cases, which indicates that none of the two irreversibility lines reproduces the observed behavior in the present case. Therefore, we fit the $T_{\text{irr}}(H)$ curve using Eq. (1) by keeping the exponent p as a free parameter, which gives $A = 0.028 \pm 0.001$ Oe$^{-0.29}$, $p = 0.29 \pm 0.03$, and $T_{\text{irr}}(0) = 20.5 \pm 0.3$ K and the best-fit curve is shown by the black solid line in Fig. 1(i). The value of the power exponent p is significantly lower than both the A-T and G-T lines, which indicates the existence of a different universality class in the present case. Kotliar and Sompolinsky theoretically redefine the A-T and G-T lines with the $D/k_B T \gg (\mu H/k_B T)^{2/3}$ and $D/k_B T \ll (\mu H/k_B T)^{5/2}$ conditions in the strong and weak anisotropic regimes, respectively, where D is the strength of the Dzyaloshinskii-Moriya interactions, k_B is the Boltzmann constant, and μ is the magnetic moment of a spin [54]. Interestingly, the authors observed the value of power exponent $p = 1/3$ in the moderate anisotropic regime, where $(\mu H/k_B T)^{5/2} \ll D/k_B T \ll \mu H/k_B T$ [54], which is close to the value obtained in the present case. Thus, we believe that the $x = 0$ sample follows a different universality class with an intermediate random anisotropy, lying between the A-T and G-T lines. A similar behavior is also reported in the other disordered compounds such as $Mn_{0.25}Ti_{1.1}S_2$ [48], $ZnTiCoO_4$ [55], and Ba_2CoRuO_6 [56].

B. Isothermal magnetization and the exchange-bias effect

To further unravel the low-temperature spin dynamics, we measure the field-dependent magnetization (M-H) curves between ± 70 kOe at 5 K for the $x = 0$ and 0.2 samples, after cooling the samples in the different magnetic fields, H_{CF}, as shown in Figs. 2(a) and 2(b), respectively. The ZFC M-H curves show the coercivity of around 930 and 520 Oe for the $x = 0$ and 0.2 samples, indicating the presence of weak but finite FM interactions in these samples, which are found to decrease with La substitution. Furthermore, the nonsaturating behavior of the M-H curves even up to 70 kOe suggests the presence of canted spins and/or local AFM coupling in both the samples. To further understand this, we fit the ZFC virgin magnetization isotherms of both the samples in the high-field region (H ⩾ 25 kOe) using the law of approach to the saturation [6,57]

$$M(H) = M_S\left(1 - \frac{a}{H} - \frac{b}{H^2}\right) + \chi_{\text{hf}}H, \tag{2}$$

where M_S is the saturation magnetization, terms a/H and b/H^2 are attributed to the structural defects and magnetocrystalline anisotropy, respectively, and χ_{hf} represents the high-field susceptibility due to the enhanced spontaneous magnetization as a result of the applied magnetic field. The best-fit curves for both the samples are shown by the solid red lines in the respective insets (a1) and (b1) of Figs. 2(a) and 2(b), which gives $M_S = 0.26$ and 0.44 μ_B/f.u. for the $x = 0$ and 0.2 samples, respectively. The calculated values of the saturation magnetization are significantly lower than the theoretical saturation moment M_S for free Co^{3+} or Co^{2+} ions ($g_J J \mu_B = 6 \mu_B$), which further confirm the local AFM
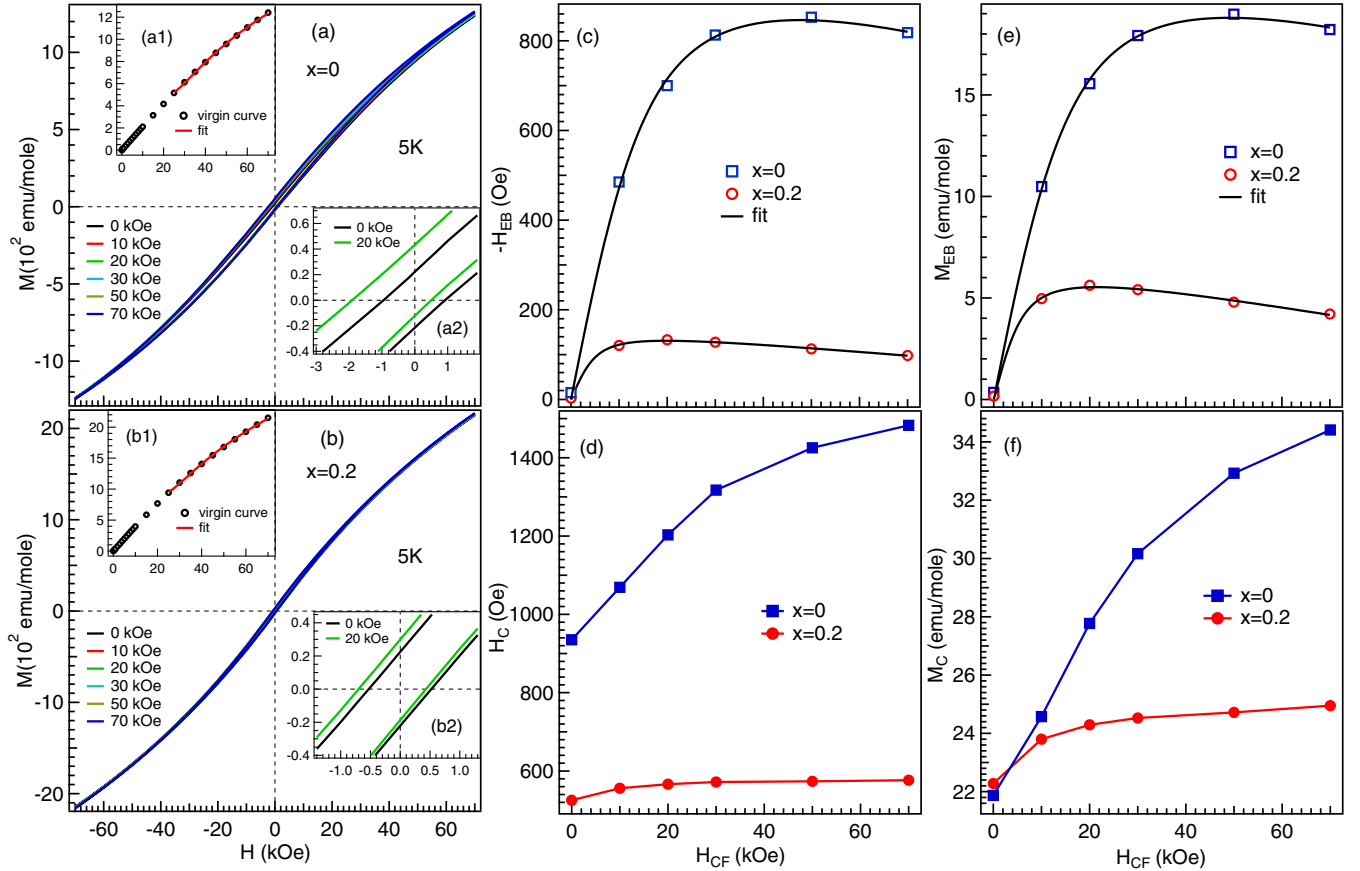
FIG. 2. The M-H curves recorded at 5 K in ZFC and FC modes for the (a) $x = 0$ and (b) 0.2 samples. Insets (a1) and (b1) show the virgin magnetization isotherms in the ZFC mode with the best fit (solid red line) using Eq. (2) in the high field (>25 kOe) regime, and insets (a2) and (b2) are the enlarged view of the low-field region for the zero-field and 20 kOe field-cooled modes, for the $x = 0$ and 0.2 samples, respectively. The cooling field, H_{CF} dependence of the (c) exchange bias field, H_{EB}, (d) coercive field, H_C, (e) exchange bias magnetization, M_{EB}, and (f) magnetic coercivity, M_C at 5 K for the $x = 0$ and 0.2 samples. The solid black lines in panels (c) and (e) represent the best fit curves using Eq. (4).

coupling or canted spins and/or the strong crystal field in these samples. The higher value of M_S in the case $x = 0.2$ as compared with the $x = 0$ sample suggests stronger FM interactions in the former. Moreover, Co^{2+} in the octahedral environment shows significant unquenched orbital magnetic moment [58–60], which can also lead to this higher magnetic moment in case of the $x = 0.2$ sample, as La substitution converts 20% Co from 3+ to 2+ [26,40].

Here, it is important to emphasize again that the mixed FM–AFM interactions result in the low-temperature cluster glass (CG) behavior of these samples [41]. Furthermore, the frustrated spins due to multiple magnetic interactions can lead to the exchange bias effect in the phase separated polycrystalline samples [5–7,61,62]. In the present case, we observe the symmetric M-H loops around the $H = 0$ axis in the ZFC mode for both the samples, which indicate the absence of the anisotropy due to the randomness at the FM–CG or AFM–CG boundaries. However, a significant shift of the M-H curves towards the negative field and positive magnetization axes is clearly observed in the FC modes, as shown in insets (a2) and (b2) of Figs. 2(a) and 2(b) for the $x = 0$ and 0.2 samples, respectively. This indicates the presence of the conventional EB effect in both the samples due to the unidirectional anisotropic exchange interactions [7,63,64]. However, the $x = 0.2$ sample

shows much lower shift in the hysteresis loop as compared with the $x = 0$ sample [see insets (a2) and (b2) of Figs. 2(a) and 2(b)], indicating the lower interfacial exchange coupling in this sample. A reduction in the size of the interacting spin cluster in case the $x = 0.2$ as compared with the $x = 0$ sample [41] may be the possible reason for this observed reduction in the EB with the La substitution.

Now we focus on the quantitative understanding of this observed shift in the hysteresis, both horizontally as well as vertically by calculating the exchange bias field [$H_{EB} = (H_{C+} + H_{C-})/2$], coercive field [$H_C = (|H_{C+}| + |H_{C-}|)/2$], exchange bias magnetization [$M_{EB} = (M_{C+} + M_{C-})/2$], and magnetic coercivity [$M_C = (|M_{C+}| + |M_{C-}|)/2$], where H_{C+} and H_{C-} are the positive (right) and negative (left) coercive fields, and M_{C+} and M_{C-} are the positive (upper) and negative (lower) remanent magnetization, respectively [6,65], as shown in Figs. 2(c)–2(f) for both the samples. Interestingly, all the four parameters decrease with the La substitution. More strikingly, the exchange bias field as well as exchange bias magnetization in case of the $x = 0$ sample increases with increase in the cooling field, then attain a saturation value around 50 kOe, and then decreases with further increase in the H_{CF} for 70 kOe. On the other hand, both of these parameters attain a saturation value at a much lower H_{CF} of around 20

kOe in case of the $x = 0.2$ sample, and then decreases for the higher values of H_{CF} [see Figs. 2(c) and 2(e)]. A similar reduction in the exchange bias parameters at the higher cooling fields is also reported in the several phase separated polycrystalline samples, which is attributed to the growth of the FM domains [5,6,61,62,66,67]. The applied H_{CF} reduces the random direction of the anisotropic exchange interactions at the FM–AFM interface by aligning the FM spins in the direction of field. Thus, the H_{EB} and M_{EB} increases with increase in H_{CF}. However, at the higher H_{CF} the FM or CG interactions dominate over the AFM coupling, causing a reduction in the EB parameters. An increment in the FM interactions and/or growth of the FM domains at the higher field is evident from the enhancement in the H_C and M_C values up to 70 kOe for both the samples [see Figs. 2(d) and 2(f)]. This can be quantitatively understood from the following EB relation developed for the AFM–FM film interfaces [1,5]:

$$-H_{EB} = J \frac{S_{AFM}S_{FM}}{\mu_0 t_{FM} M_{FM}}, \tag{3}$$

where J is the exchange integral per unit area at the FM–AFM interface, S_{AFM} and S_{FM} are the magnetization at the AFM and FM interfaces, respectively, t_{FM} and M_{FM} are the thickness and magnetization of the FM film, respectively. The increase in H_{CF} enhances the interfacial magnetization S_{AFM} and S_{FM} as well as t_{FM} and M_{FM} due to growth and alignment of the FM domains, respectively, which causes an overall enhancement in H_{EB}. However, at the higher H_{CF}, the FM clusters grow in size, which decreases the FM–AFM interface area and hence the values of S_{AFM} and S_{FM} accompanied by enhancement in the t_{FM} and M_{FM}. Therefore, the H_{EB} decreases for the strong enough H_{CF} [Eq. (3)].

It is clear from the above discussion that the value of this critical cooling field H_{CF}^{crit} above which H_{EB} decreases depends on the strength of the exchange interactions at the FM–AFM interface. Therefore, to further understand this, the cooling-field dependence of the EB field is expressed using the following relation, given by Niebieskikwiat and Salamon for $\mu_0 H_{CF} < k_B T$ [5,18,68]:

$$-H_{EB} \propto J \left[\frac{J\mu_0}{(g\mu_B)^2} L \left(\frac{\mu H_{CF}}{k_B T_f} \right) + H_{CF} \right], \tag{4}$$

where J is the exchange integral at the FM–AFM interface, $\mu_0 = 4.0 \mu_B$ and $3.8 \mu_B$ for the $x = 0$ and 0.2 samples, respectively [4.0 μ_B for HS Co^{3+} ($S = 2$) and 3.0 μ_B for HS Co^{2+} ($S = 3/2$) ions], μ_B is the Bohr magneton, $g = 2$ is the Landé g factor, L represents the Langevin function, $\mu = N\mu_0$ is the ferromagnetic moment, N is the number of spins in a ferromagnetic cluster, k_B is Boltzmann's constant, and T_f is the freezing temperature below which FM–AFM clusters coexist. For the smaller values of H_{CF} the first term in Eq. (4) dominates, i.e., $H_{EB} \propto J^2$, whereas for the higher cooling field, the second term dominates, i.e., $H_{EB} \propto J$. So, for the negative value of J, H_{EB} is expected to first increase with H_{CF} and then decrease at the higher values where the second term starts dominating over the first, which can even change the sign of the H_{EB} [69–72]. This indicates that the observed behavior of the H_{EB} and M_{EB} in the present case can be well understood using the above model. Therefore, we fit the H_{EB} and M_{EB} as a function of H_{CF} using Eq. (4) by taking $T_f = 13.5$ and

9.7 K for $x = 0$ and 0.2, respectively [41], and varying N, J, and a proportionality constant. The best-fit curves, represented by the solid black lines in Figs. 2(c) and 2(e), exhibit an excellent agreement with the experimental data, which gives $J = -1.6 \pm 0.1$ and -0.89 ± 0.01 meV, and $N = 6 \pm 1$ and 13 ± 1 for the $x = 0$ and 0.2 samples, respectively. It is important to note that the FM clusters are two times larger in case of the $x = 0.2$ sample, which results in the smaller effective FM–AFM interface and hence a lower J value as compared with the $x = 0$ sample. These reduced FM–AFM boundaries which are necessary for the spin pinning and hence the EB effect is responsible for the observed lower values of H_{EB} and M_{EB} in case of the $x = 0.2$ sample. Moreover, for the $x = 0.2$ sample the larger FM cluster results in the more prominent effect of the increase in H_{CF} and consequently reduction in H_{EB} and M_{EB} at a much lower H_{CF} as compared with $x = 0$. The negative J value for both the samples indicate the presence of AFM coupling between the FM domains, causing the observed EB effect.

The virgin magnetization isotherms are shown in Figs. 3(a) and 3(b) for both the samples ($x = 0$ and 0.2) after cooling them in the different magnetic fields. Note that cooling the samples in an applied magnetic field from 300 K (paramagnetic region, where spins are free to align) to 5 K results in the blocking of the aligned spins in the direction of H_{CF} due to their glassy ground state [41]. This causes a remanent magnetization in these samples at $H = 0$ Oe. This zero-field magnetization M_0 resulting from the blocked spins at the FM–AFM interface can be responsible for the observed EB effect in these samples. Figure 3(c) shows the variation of the zero-field magnetization as a function of the cooling field, H_{CF}. M_0 of the $x = 0$ sample increases rapidly with increasing H_{CF} up to ≈30 kOe and then shows almost a saturating behavior with further increase up to 70 kOe. On the other hand, M_0 increases up to 20 kOe and then slightly but monotonically decreases at the higher H_{CF} in case of the $x = 0.2$ sample. As discussed above, the presence of a larger FM cluster in the $x = 0.2$ sample results in the lesser blocking of the spins at the FM–AFM interface, which lowers the value of M_0. Moreover, the high cooling field further enhances the FM interactions or grains causing the observed reduction in the M_0 for the $x = 0.2$ sample for $H_{CF} > 20$ kOe.

To further understand the effect of frozen spins on the EB phenomena, we plot the positive and negative coercivity and remanent magnetization separately in Figs. 4(a)–4(d) for both the samples. It is interesting to note that, in the case of the $x = 0$ sample, the negative (left) coercivity (H_{C-}) value increases with increasing the cooling field up to 70 kOe, whereas the positive (right) coercivity (H_{C+}) first decreases up to 20 kOe and then starts increasing with further increase in H_{CF}, as shown in Fig. 4(a). This enhancement in the H_{C+} at the higher magnetic fields is responsible for the observed reduction in the H_{EB} for $H_{CF} > 50$ kOe in this sample [see Fig. 2(a)]. On the other hand, the negative (positive) coercivity increases (decreases) up to around 20 kOe and then there is slight decrease (significant increase) in their values at $H_{CF} > 20$ kOe for the $x = 0.2$ sample. This indicates that the rate of increment in the positive coercivity is higher than the reduction rate in the negative coercivity for $H_{CF} > 20$ kOe [see Fig. 4(b)]. The larger FM domains in case of the $x = 0.2$
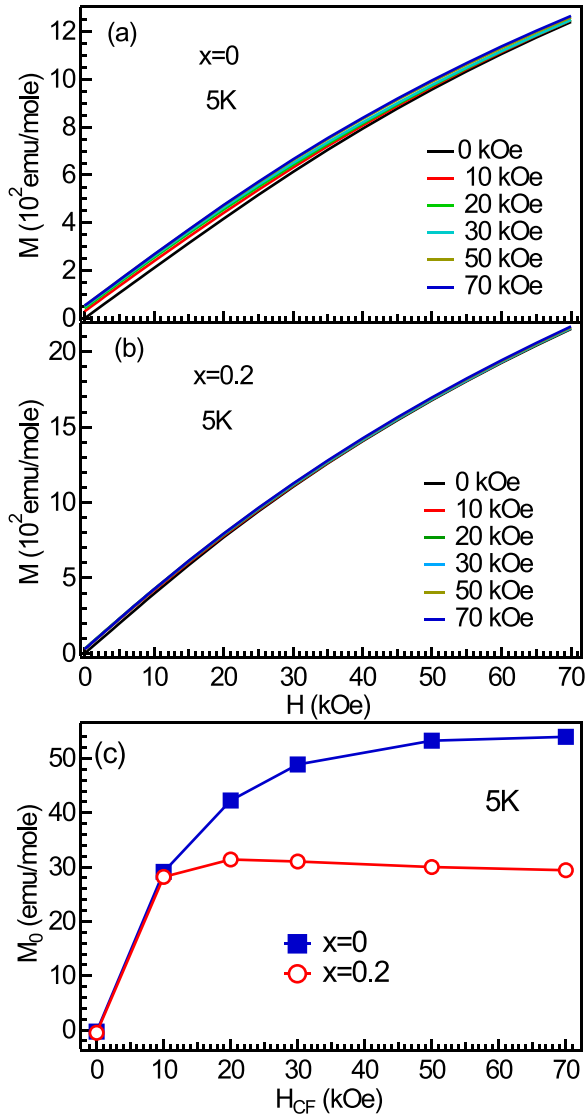
FIG. 3. (a), (b) The virgin magnetization isotherms at 5 K in different field-cooled states for the $x = 0$ and 0.2 samples, respectively. (c) The zero-field magnetization M_0 as a function of the cooling field for both samples.
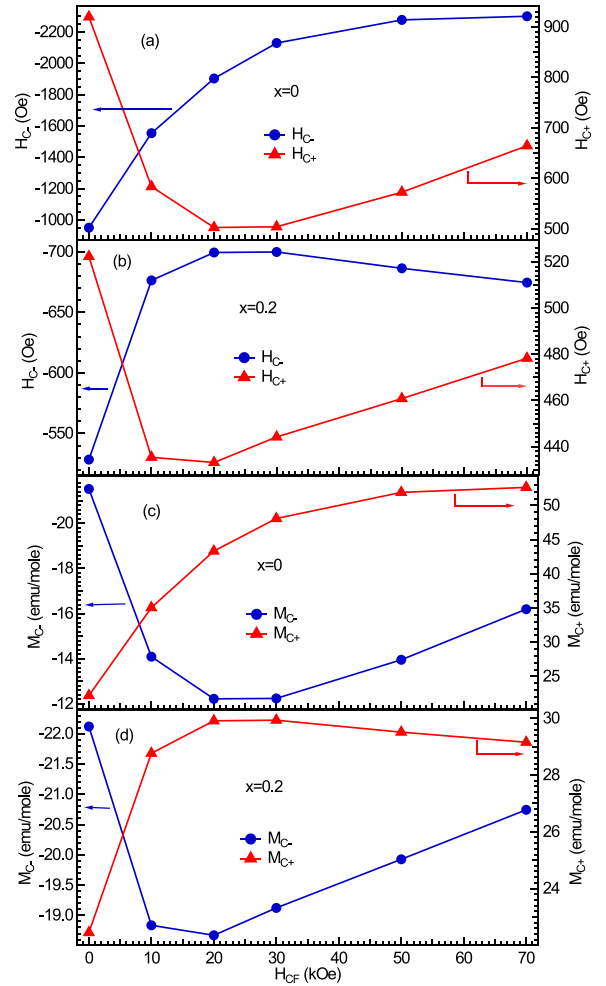

FIG. 4. (a), (b) The cooling field dependence of the negative (on left axis) and positive (on right axis) coercive fields, and (c), (d) the values of remanent magnetization, for both the samples.

as compared with the $x = 0$ sample is responsible for the observed reduction in the M_0 and consequently the decrease (increase) in H_{C-} (H_{C+}), and hence the decay of the EB effect for $H_{CF} > 20$ kOe. Moreover, the positive coercivity is found to be more responsible for such deterioration in the EB effect at the higher cooling fields for both samples. Furthermore, the M_{C-} and M_{C+} exhibit behavior analogous to that of H_{C+} and H_{C-}, respectively [see Figs. 2(c) and 2(d)]. In a typical field cycle of the M-H loop, the M_{C+} and M_{C-} are followed by H_{C-} and H_{C+}, respectively, resulting in their similar response to the blocked spins and, consequently, H_{CF}.

C. Training effect

It is important to understand the evolution of the anisotropic exchange interactions and hence the EB parameters with the M-H cycles in these samples. Therefore, we

perform the training effect measurements on both the samples, where we first cool the samples down to 5 K in the presence of 50 kOe magnetic field, and then record the consecutive M-H curves, as the enlarged view shows in Figs. 5(a) and 5(b) for the $x = 0$ and 0.2 samples, respectively. A gradual reduction in the EB effect is clearly visible for both the samples, which can be understood in terms of the demagnetization of the AFM or CG spins at the magnetically disordered interface and hence decrease in the unidirectional anisotropy with the field cycles [73]. The continuous cycling of the magnetic field results in the relaxation of the blocked spins at the domain boundaries. Note that the negative (positive) coercivity (remanent magnetization) changes much faster as compared with the positive (negative) branch for both the samples [see Figs. 5(a) and 5(b)]. However, this effect is more prominent in case of the $x = 0$ sample as compared with the $x = 0.2$. For the quantitative analysis, the positive and negative coercive field and remanent magnetization are plotted for both the samples in Figs. 5(c)–5(f). These plots show that the negative (positive) coercivity (remanent magnetization) decays rapidly within the first three to four cycles and then show almost saturating behavior. On the other hand, positive (negative)
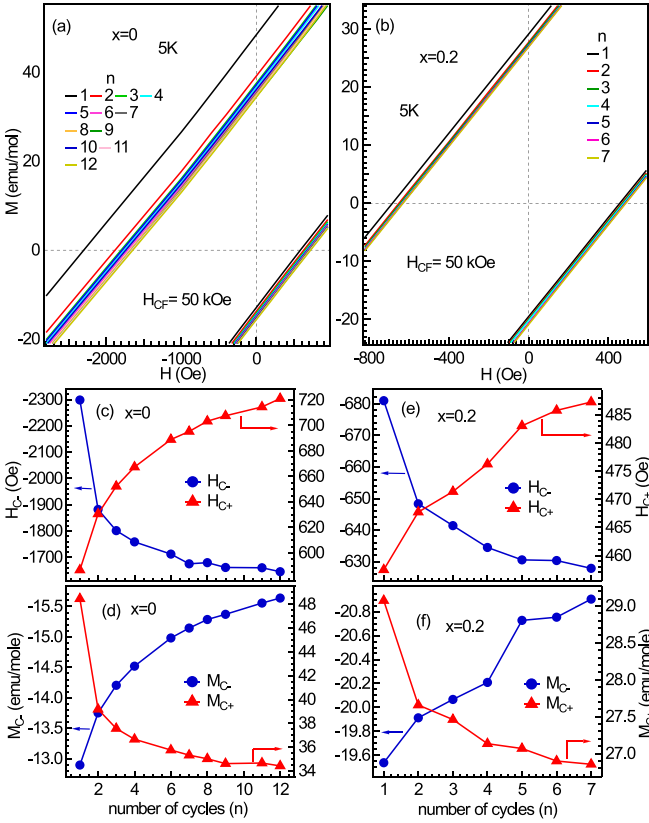
FIG. 5. The enlarged view of the *M-H* curves consecutively recorded after cooling the (a) $x = 0$ and (b) 0.2 samples in 50 kOe magnetic field at 5 K. The variation in the negative (on left axis) and positive (on right axis) coercive fields and remanent magnetization with the number of field cycles for the (c), (d) $x = 0$ and (e), (f) 0.2 samples, respectively.

coercivity (remanent magnetization) decays slowly and show a much lesser tendency to saturate even after several cycles. This behavior is consistent with the reports in Refs. [5,74,75], where the asymmetric training effect is attributed to the dominance of the thermal activation in the FM region. The domains in the SG or AFM regions may get switched due to thermal activation along each branch of the loop [74,75].

To quantitatively understand the nature of these glassy magnetic interactions, first we fit the variation of the EB field and the EB magnetization with the number of recorded *M-H* loops using the power law [76], as below:

$$H_{EB}^n - H_{EB}^\infty = \frac{k_H}{\sqrt{n}} \text{ for } n > 1, \qquad (5)$$

$$M_{EB}^n - M_{EB}^\infty = \frac{k_M}{\sqrt{n}} \text{ for } n > 1, \qquad (6)$$

where n is the number of recorded *M-H* loops, H_{EB}^∞ and M_{EB}^∞ are the values of H_{EB} and M_{EB} for $n = \infty$, and k_H and k_M are the constants. Figs. 6(a) and 6(b), show the variation in H_{EB} (left axis) and M_{EB} (right axis) with $1/\sqrt{n}$ for the $x = 0$ and 0.2 samples, respectively, where the black solid lines represent the best fit using the power law for the $n > 1$, as equations (5) and (6) are not valid for the first cycle. The best fit parameters are summarized in Table I, which show a significant decrease in the H_{EB}^∞ (M_{EB}^∞) and k_H (k_M) with the La

substitution, indicating a reduction in the EB effect. Furthermore, the power law underestimate the values of both H_{EB} and M_{EB} for $n = 1$, as shown by the red dashed lines in Figs. 6(a) and 6(b) for the $x = 0$ and 0.2 samples, respectively. However, this effect is more prominent in case of the $x = 0$ sample. A steep decrease in the H_{EB} or M_{EB} between the first and second cycles is usually related with the relaxation of the spins at the disordered interfaces due to the surface drag from the switching field, whereas a gradual decrease in the exchange bias parameters is attributed to the relaxations of the thermally activated spins during the consecutive field cycles and follow the power-law behavior [74,77]. A smaller deviation in the EB parameters from the power law at $n = 1$ in case of the $x = 0.2$ sample indicate the more thermal relaxation of the pinned spins during the initial field cycles as compared with the $x = 0$ sample.

The training effect data can be analyzed using the spin-relaxation model proposed by C. Binek [78], which suggest the demagnetization of the non-FM spins at the disordered interface with the field cycling. In this model, the H_{EB} and M_{EB} can be expressed as a function of n using the following recursive formulas [78]:

$$H_{EB}(n + 1) - H_{EB}(n) = -\gamma_H \left[H_{EB}(n) - H_{EB}^\infty \right]^3, \qquad (7)$$

$$M_{EB}(n + 1) - M_{EB}(n) = -\gamma_M \left[M_{EB}(n) - M_{EB}^\infty \right]^3, \qquad (8)$$

where γ_H and γ_M are the constants. The H_{EB} and M_{EB} curves are generated using the above equations by taking the experimental $H_{EB}(1)$ and $M_{EB}(1)$ data, and the values of γ_H, H_{EB}^∞, γ_M, and M_{EB}^∞ as given in Table I. These results are presented by the solid symbols in Figs. 6(c) and 6(d) for the $x = 0$ and 0.2 samples, respectively, where a good agreement between the experimental and the generated data [using equations (7) and (8)] is clearly observed even for the $n = 1$. Also, we observe a reduction in the values of H_{EB}^∞ and M_{EB}^∞ with the La substitution analogous to the power law, discussed above. Furthermore, the values of γ_H and γ_M significantly increase with the La substitution. Note that $\gamma_H = $ b/K$^2\xi$, where b and ξ are different constants, and by putting $K = -JS_{FM}/M_{FM}t_{FM}$ in Eq. (3), we can write $H_{EB} = KS_{AFM}/\mu_0$ [1,5,78]. Thus, the observed enhancement in the value of γ_H indicate the lower value of K, and hence the H_{EB} value in case of the $x = 0.2$ sample. However, this model slightly underestimate the values of H_{EB}^∞ and M_{EB}^∞ as compared with that extracted from the power law (see Table I), which is also observed in Ref. [74].

Therefore, we further analyze the training effect data using the model proposed in Ref. [79], which consider the two different types of uncompensated spins, namely, frozen and rotating spins at the disordered interface having different relaxation times, where H_{EB} and M_{EB} can be expressed as a function of n as below:

$$H_{EB}^n = H_{EB}^\infty + A_f \exp\left(\frac{-n}{p_f}\right) + A_r \exp\left(\frac{-n}{p_r}\right), \qquad (9)$$

$$M_{EB}^n = M_{EB}^\infty + A_f \exp\left(\frac{-n}{p_f}\right) + A_r \exp\left(\frac{-n}{p_r}\right), \qquad (10)$$

where the pre-exponential factor A represents the weight factors having dimensions of magnetic field, the dimensionless parameters p are the measure of the relaxation times, and
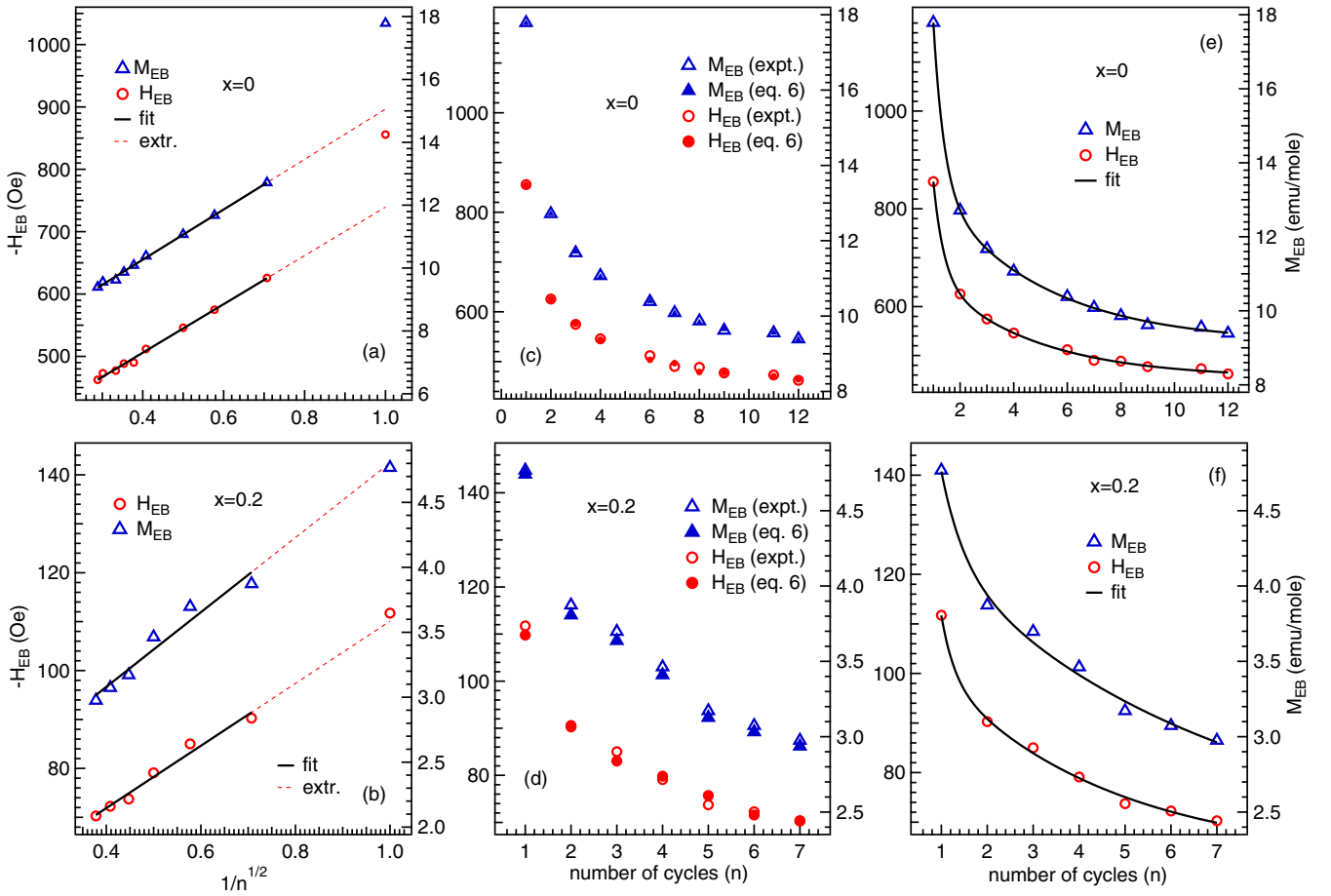
FIG. 6. (a), (b) The EB field (H_{EB}; on left axis) and EB magnetization (M_{EB}; on right axis) versus $1/\sqrt{n}$ plot for the $x = 0$ and 0.2 samples, respectively. The black solid lines represent the power-law fit of the data for $n > 1$ and the red dashed lines represent the extrapolation of the data to $n = 1$. (c), (d) The dependence of H_{EB} and M_{EB} on the number of field cycles, where empty and solid symbols represent the experimental and generated data from Eqs. (7) and (8), respectively. (e), (f) The best fit (solid black lines) of the H_{EB} and M_{EB} versus n data using Eqs. (9) and (10) for the $x = 0$ and 0.2 samples, respectively.

the subscripts f and r represent the frozen and rotatable spin components, respectively. The solid black lines in Figs. 6(e) and 6(f) show the best fit of H_{EB} and M_{EB} curves for the $x = 0$ and 0.2 samples, respectively, using the above model and the fitting parameters are given in Table I. We find that the weight factors A_f and A_r decreases with the La substitution, which indicate the reduction in the concentration of both frozen as well as rotatable spins at the disordered interface with x. Furthermore, it can be inferred from Table I that the rotatable components relax 10 and 13 times faster than the frozen spin

component for the $x = 0$ and 0.2 samples, respectively. This indicates that the rotatable spins play a dominating role in governing the EB effect as a function of n. Now, we calculate the relative percentage of reduction in the EB effect [TE(%)] with the number of field cycles (n) using the following relation [7,80]:

$$\text{TE}(\%) = \left[1 - \frac{\left(H_{EB}^1 - H_{EB} \right)^n}{H_{EB}^1} \right] \times 100\%. \quad (11)$$

TABLE I. The parameters extracted by fitting the training effect data of the $x = 0$ and 0.2 samples using Eqs. (5)–(10).

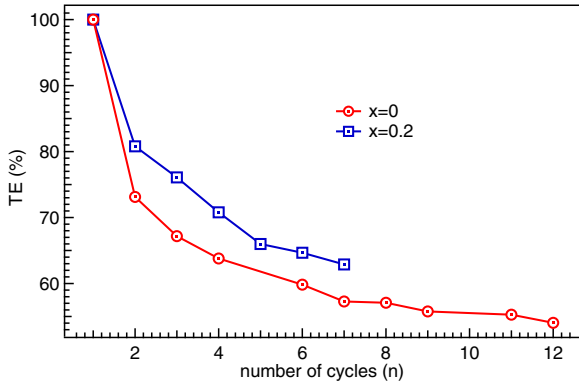| Fit using equation(s)		$x = 0$					$x = 0.2$			
H_{EB} and M_{EB} by (5) and (6)	H_{EB}^∞	k_H	M_{EB}^∞	k_M			H_{EB}^∞	k_H	M_{EB}^∞	k_M
	−350(4)	389(9)	7.1(1)	8.0(1)			−46(2)	64(5)	1.9(2)	2.9(3)
H_{EB} and M_{EB} by (7) and (8)	H_{EB}^∞	γ_H	M_{EB}^∞	γ_M			H_{EB}^∞	γ_H	M_{EB}^∞	γ_M
	−281(18)	1.21×10^{-6}	5.6(1)	2.8×10^{-3}			−40(6)	5.8×10^{-5}	1.7(4)	3.0×10^{-2}
H_{EB} by (9)	H_{EB}^∞	A_f	P_f	A_r	P_r	H_{EB}^∞	A_f	P_f	A_r	P_r
	−454(7)	−2498(47)	0.39(9)	−264(28)	3.8(6)	−62(5)	−420(11)	0.28(2)	−48(3)	3.7(7)
M_{EB} by (10)	M_{EB}^∞	A_f	P_f	A_r	P_r	M_{EB}^∞	A_f	P_f	A_r	P_r
	9.1(1)	54(16)	0.41(6)	5.2(3)	4.1(5)	2.3(2)	5.5(1)	0.5(1)	2.2(2)	6.1 (1)

FIG. 7. The relative percentage reduction in the training effect [Eq. (11)] with the number of field cycles (n) for the $x = 0$ and 0.2 samples.

In Fig. 7 we find that the TE(%) value decreases to the 73% and 81% of its initial value only after the first field cycling (H_{EB}^2) in case of the $x = 0$ and 0.2 samples, respectively. It is clear from Fig. 7 that, despite the significantly lower H_{EB} [see Fig. 2(c)], the $x = 0.2$ sample shows the much stable EB effect with the field cycling as compared with the $x = 0$ sample. For example, the H_{EB} reduces to the 57% of its initial value (H_{EB}^1) in case of the $x = 0$ sample, whereas retains 63% in the $x = 0.2$ sample at the seventh cycle. The lower effective FM–AFM disordered interface decrease the probability of the relaxation of uncompensated spins with the field cycles, resulting in the relatively robust EB effect in case of the $x = 0.2$ as compared with the $x = 0$ sample.

D. Origin and evolution of the exchange-bias effect

It is important to mention that the Co is present predominantly in 3+ valence state in the $x = 0$ sample [40], which excludes the possibility of the competing magnetic interactions due to the multiple valence states of Co as the origin of the observed EB effect in this sample. The XRD, EXAFS, and ND measurements indicate that Co^{3+} and Nb^{5+} (nonmagnetic) ions can swap between their given Wyckoff positions, as shown in Fig. 8(a), resulting in the Co^{3+}-O-Co^{3+} exchange interactions in case of the $x = 0$ sample [26,38,40]. Moreover, the high-resolution electron microscopic measurements reported in Ref. [38] suggest the presence of some ordered domains at nanoscale range, which give rise to the additional Co^{3+}-O-Nb^{5+}-O-Co^{3+} channels. Furthermore, depending on the relative strength of the crystal field and Hund's exchange energy, the Co^{3+} can exist in the different spin states, namely, low spin (LS, $t_{2g}^6 e_g^0$; $S = 0$), intermediate spin (IS, $t_{2g}^5 e_g^1$; $S = 1$) and/or high spin (HS, $t_{2g}^4 e_g^2$; $S = 2$) state, resulting in the complex magnetic interactions in this sample [26]. For example, Goodenough–Kanamori rules predict LS Co^{3+}–O–HS Co^{3+} interactions as FM and HS Co^{3+}–O–HS Co^{3+} as AFM in nature [81,82]. Therefore, the presence of these competing magnetic interactions of varying sign and strength arising from the different spin states of Co^{3+} give rise to the frustration in the spins and consequently cluster-glass-like behavior and EB effect in the $x = 0$ sample having only one magnetic atom with a fix valence state [41].

However, the substitution of La^{3+} ions at the Sr^{2+} site transforms the Co from 3+ to 2+ state in the same proportion [40] and monotonically enhance the B-site ordering, and hence the $Co^{3+/2+}$-O-Nb^{5+}-O-$Co^{3+/2+}$ interaction channels in $Sr_{2-x}La_xCoNbO_6$ samples [26,40–42]. We observe the reduction in the coercivity, but at the same time an enhancement in the saturation magnetization (M_S) values in the $x = 0.2$ as compared with the $x = 0$ sample, see the insets of Figs. 2(a) and 2(b). An increase in the size of the FM cluster, as discussed above, may be responsible for the observed enhancement in the M_S value, whereas a decrease in the
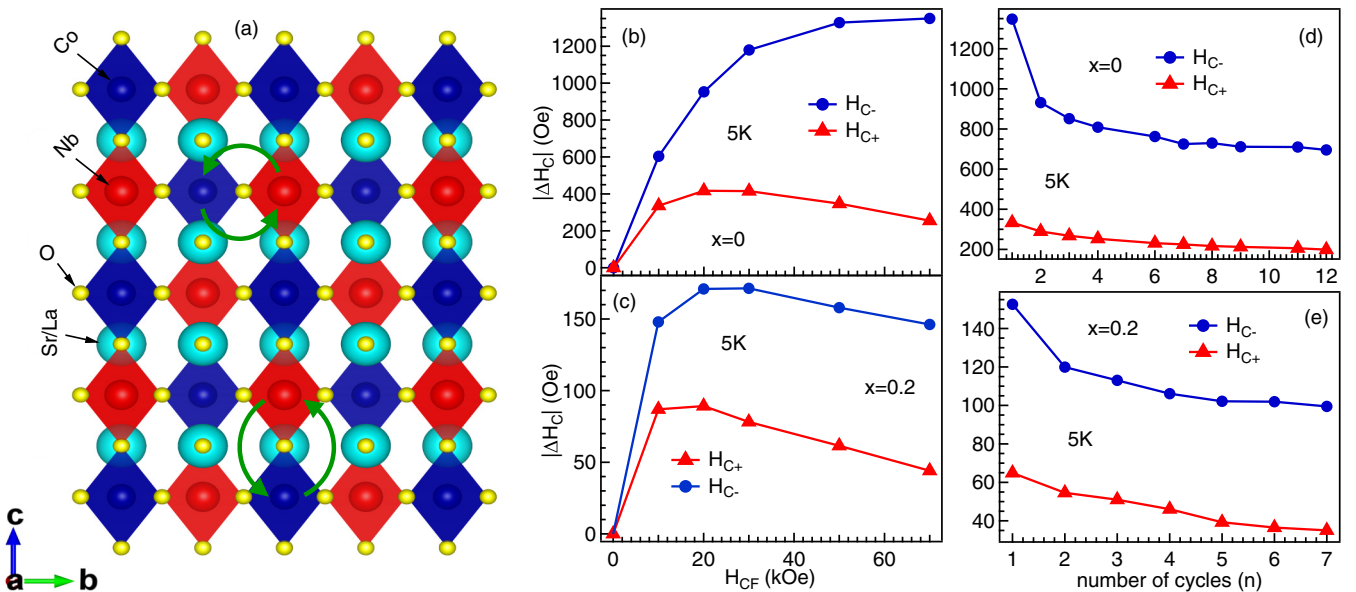

FIG. 8. (a) A three-dimensional schematic of the Sr_2CoNbO_6 crystal structure where the arrows indicate the possible disorder paths in the crystal. (b), (c) The variation of the position and negative coercivity with respect to the zero-field coercivity as function of cooling field, and (d), (e) the number of field cycles after cooling the samples in 50 kOe field at 5 K for the $x = 0$ and 0.2 samples, respectively.

coercivity suggest the reduction in the strength of these FM interactions in the $x = 0.2$ sample. Recently, a significantly larger EB effect is reported in $SrLaFe_{0.5}(Mn_{0.25}Co_{0.25})O_4$ as compared with the $SrLaFe_{0.25}(Mn_{0.25}Co_{0.5})O_4$ in spite of the smaller coercivity of the former, indicating the dominating contribution of the effective CG-AFM interface in governing the EB effect [7]. The larger FM cluster reduces the frustrated spins at the FM–CG or FM–AFM interfaces and hence lower EB effect in the $x = 0.2$ sample. Moreover, we recently reported that the size of the glassy spin cluster decreases with the La substitution in $Sr_{2-x}La_xCoNbO_6$ samples for the $x \leqslant 0.4$ [41], which can also play a key role in reducing the EB effect in case of the $x = 0.2$. The larger FM and smaller CG domains also reduce the critical cooling field (H_{CF}^{crit}), above which the H_{EB} starts deceasing, from 50 kOe in case of the $x = 0$ to 20 kOe for the $x = 0.2$ sample.

More importantly, we observe the asymmetric exchange bias effect in both the field-cooled M-H curves with varying H_{CF} as well as in the training effect measurements. The reduction in the EB parameters at the higher cooling field was found to be mainly governed by the H_{C+} (M_{C-}) branch; on the other hand, the training effect was controlled by the H_{C-} (M_{C+}) branch. To understand this, we plot the magnitude of change in the positive and negative zero-field coercivity with respect their field cooled values (shift in the individual branches) as a function of H_{CF} and n for both the samples in Figs. 8(b)–8(e). It is interesting to note that the shift in the negative branch in the field cooled M-H is significantly higher as compared with the positive branch in both the samples [see Figs. 8(b) and 8(c)]. The lower shifting of the positive branch is attributed to the relaxation of the locked spins during the first half of the field cycling. Moreover, a significantly higher shift in the negative coercivity signifies that the enhancement in the H_C due to enhancement (growth) in the ferromagnetic interactions (domains) with the cooling field is mainly attributed to the H_{C-}. In the case of the $x = 0$ sample, the change in negative coercivity increases with increase in the cooling field up to 70 kOe, whereas the positive coercivity decreases for $H_{CF} > 20$ kOe [see Fig. 8(b)]. This clearly indicates the different influence of the cooling field on the two branches. On the other hand, the change in both the coercivities decreases for $H_{CF} > 20$ kOe in case of the $x = 0.2$ sample [see Fig. 8(c)], i.e., the M-H loops start shifting back to the right side for $H_{CF} > 20$ kOe in this sample. This effect is more prominent in the positive branch. Furthermore, we observe an unequal shift of the two branches of the M-H loop and their different

evolution with the field cycles, as shown in Figs. 8(d) and 8(e), which is responsible for the asymmetric training effect observed in both the samples. However, this effect is less prominent in case of the $x = 0.2$ as compared with the $x = 0$, which results in the more stable EB effect in the former.

IV. CONCLUSIONS

The influence of antisite disorders on the EB effect of $Sr_{2-x}La_xCoNbO_6$ ($x = 0, 0.2$) samples is investigated in detail using the FC M-H and training effect data analysis. The field dependence of the T_{irr} deviates from both the AT and GT lines, which suggest the presence of different universality class with the moderate unidirectional exchange interactions in the $x = 0$ sample. A significant reduction in the EB effect is observed in case of the $x = 0.2$ sample due to the larger FM and smaller CG domains as compared with the $x = 0$ sample. The EB effect show a notable reduction at the higher H_{CF} for both the samples and the positive (negative) coercivity (remanent magnetization) is found to predominantly govern this effect. Furthermore, both the samples show the asymmetric training effect, which is mainly governed by the negative coercivity branch. The analysis of the decay in the EB effect with the M-H cycles shows that the rotatable spins relax 10 and 13 times faster than the frozen spins at the disordered interfaces of the $x = 0$ and 0.2 samples, respectively. Through the training effect measurements, we reveal a much more stable EB effect with the M-H cycles for the $x = 0.2$ sample as compared with that of the $x = 0$. We observe a direct correlation between the EB effect and antisite disorders, where the latter, and consequently the former, can be precisely controlled as a function of La substitution in these compounds. Therefore, the detailed investigation of the low-temperature spin dynamics responsible for systematic tuning of the EB effect with the La substitution in these samples can be useful to engineer suitable candidates for the desired applications.

ACKNOWLEDGMENTS

---

[1] W. H. Meiklejohn and C. P. Bean, New magnetic anisotropy, Phys. Rev. **102**, 1413 (1956).

[2] R. L. Stamps, Mechanisms for exchange bias, J. Phys. D: Appl. Phys. **33**, R247 (2000).

[3] M. Vasilakaki and K. N. Trohidou, Numerical study of the exchange-bias effect in nanoparticles with ferromagnetic core/ferrimagnetic disordered shell morphology, Phys. Rev. B **79**, 144402 (2009).

[4] A. E. Berkowitz, G. F. Rodriguez, J. I. Hong, K. An, T. Hyeon, N. Agarwal, D. J. Smith, and E. E. Fullerton, Antiferromagnetic

MnO nanoparticles with ferrimagnetic Mn_3O_4 shells: Doubly inverted core-shell system, Phys. Rev. B **77**, 024403 (2008).

[5] S. Karmakar, S. Taran, E. Bose, B. K. Chaudhuri, C. P. Sun, C. L. Huang, and H. D. Yang, Evidence of intrinsic exchange bias and its origin in spin-glass-like disordered $L_{0.5}Sr_{0.5}MnO_3$ manganites (L = Y, $Y_{0.5}Sm_{0.5}$, and $Y_{0.5}La_{0.5}$), Phys. Rev. B **77**, 144409 (2008).

[6] R. C. Sahoo, Y. Takeuchi, O. Ohtomo, and Z. Hossain, Exchnage bias and spin glass states driven by antisite disorder in the

double perovskite compound LaSrCoFeO$_6$, Phys. Rev. B **100**, 214436 (2019).

[7] V. K. Anusree, R. R. Das, P. Neenu Lekshmi, R. Dhal, C. V. Colin, and P. N. Santhosh, Giant exchange bias effect in Ruddlesden-Popper oxides SrLaFe$_{0.25+x}$Mn$_{0.25}$Co$_{0.5-x}$O$_4$ ($x0$, 0.25): Role of the cluster glass magnetic phase in a quasi-two-dimensional perovskite, Phys. Rev. B **102**, 134405 (2020).

[8] V. Kuncser, M. Valeanu, G. Schinteie, G. Filoti, I. Mustata, C. P. Lungu, A. Anghel, H. Chiriac, R. Vladoiu, and J. Bartolome, Exchange bias and spin valve systems with Fe-Mn antiferromagnetic pinning layers, obtained by the thermo-ionic vacuum arc method, J. Magn. Magn. Mater. **320**, e226 (2008).

[9] J. Sort, S. Suriñach, J. S. Muñoz, M. D. Baró, J. Nogués, G. Chouteau, V. Skumryev, and G. C. Hadjipanayis, Improving the energy product of hard magnetic materials, Phys. Rev. B **65**, 174420 (2002).

[10] A. López-Ortega, M. Estrader, G. Salazar-Alvarez, A. G. Roca, and J. Nogués, Applications of exchange coupled bi-magnetic hard/soft and soft/hard magnetic core/shell nanoparticles, Phys. Rep. **553**, 1 (2015).

[11] X. He, Y. Wang, N. Wu, A. N. Caruso, E. Vescovo, K. D. Belashchenko, P. A. Dowben, and C. Binek, Robust isothermal electric control of exchange bias at room temperature, Nat. Mater. **9**, 579 (2010).

[12] M. Liu, J. Lou, S. Li, and N. X. Sun, E-field control of exchange bias and deterministic magnetization switching in AFM/FM/FE multiferroic heterostructures, Adv. Funct. Mater. **21**, 2593 (2011).

[13] S. A. Wolf, D. D. Awschalom, R. A. Buhrman, J. M. Daughton, S. Von Molnár, M. L. Roukes, A. Y. Chtchelkanova, and D. M. Treger, Spintronics: A spin-based electronics vision for the future, Science **294**, 1488 (2001).

[14] C. Binek, A. Hochstrat, X. Chen, P. Borisov, W. Kleemann, and B. Doudin, Electrically controlled exchange bias for spintronic applications, J. Appl. Phys. **97**, 10C514 (2005).

[15] R. A. Murphy, L. E. Darago, M. E. Ziebel, E. A. Peterson, E. W. Zaia, M. W. Mara, D. Lussier, E. O. Velasquez, D. K. Shuh, J. J. Urban, J. B. Neaton, and J. R. Long, Exchange bias in a layered metal-organic topological spin glass, ACS Cent. Sci. **7**, 1317 (2021).

[16] M. Ali, P. Adie, C. H. Marrows, D. Greig, B. J. Hickey, and R. L. Stamps, Exchange bias using a spin glass, Nat. Mater. **6**, 70 (2007).

[17] T. Motohashi, V. Caignaert, V. Pralong, M. Hervieu, A. Maignan, and B. Raveau, Competition between ferromagnetism and spin glass: The key for large magnetoresistance in oxygen-deficient perovskites SrCo$_{1-x}$$M_xO_{3-\delta}$ (M = Nb, Ru), Phys. Rev. B **71**, 214424 (2005).

[18] I. Fita, I. O. Troyanchuk, T. Zajarniuk, P. Iwanowski, A. Wisniewski, and R. Puzniak, Exchange bias effect and Griffiths phase coexistence in the disordered cobaltite Gd$_{0.5}$Sr$_{0.5}$CoO$_{3-\delta}$, Phys. Rev. B **98**, 214445 (2018).

[19] R. Shukla and R. S. Dhaka, Anomalous magnetic and spin glass behavior in Nb substituted LaCo$_{1-x}$Nb$_x$O$_3$, Phys. Rev. B **97**, 024430 (2018).

[20] R. Shukla, Anil Jain, M. Miryala, M. Murakami, K. Ueno, S. M. Yusuf, and R. S. Dhaka, Spin dynamics and unconventional magnetism in insulating La$_{(1-2x)}$Sr$_{2x}$Co$_{(1-x)}$Nb$_x$O$_3$, J. Phys. Chem. C **123**, 22457 (2019).

[21] B. Yan, A. K. Paul, S. Kanungo, M. Reehuis, A. Hoser, D. M. Többens, W. Schnelle, R. C. Williams, T. Lancaster, F. Xiao, J. S. Möller, S. J. Blundell, W. Hayes, C. Felser, and M. Jansen, Lattice-site-specific spin dynamics in double perovskite Sr$_2$CoOsO$_6$, Phys. Rev. Lett. **112**, 147202 (2014).

[22] R. Shukla and R. S. Dhaka, Evolution of complex magnetic phases and metal-insulator transition through Nb substitution in La$_{0.5}$Sr$_{0.5}$Co$_{1-x}$Nb$_x$O$_3$, Phys. Rev. B **107**, 165108 (2023).

[23] S. Vasala and M. Karppinen, $A_2B'B''O_6$ perovskites: A review, Prog. Solid State Chem. **43**, 1 (2015).

[24] A. Kumar, A. Senyshyn, and D. Pandey, Evidence for cluster spin glass phase with precursor short-range antiferromagnetic correlations in the B-site disordered Ca(Fe$_{1/2}$Nb$_{1/2}$)O$_3$ perovskite, Phys. Rev. B **99**, 214425 (2019).

[25] G. R. Haripriya, C. M. N. Kumar, R. Pradheesh, L. M. Martinez, C. L. Saiz, S. R. Singamaneni, T. Chatterji, V. Sankaranarayanan, K. Sethupathi, B. Kiefer, and H. S. Nair, Contrasting the magnetism in La$_{2-x}$Sr$_x$FeCoO$_6$ (x = 0, 1, 2) double perovskites: The role of electronic and cationic disorder, Phys. Rev. B **99**, 184411 (2019).

[26] A. Kumar and R. S. Dhaka, Unraveling magnetic interactions and the spin state in insulating Sr$_{2-x}$La$_x$CoNbO$_6$, Phys. Rev. B **101**, 094434 (2020).

[27] M. Das, P. Dutta, S. Giri, S. Majumdar, A. Bandyopadhyay, A. K. Yadav, S. N. Jha, D. Bhattacharyya, G. Das, and V. Rajaji, Cationic disorder: A pathway for demonstrating inverse exchange bias in Gd$_2$CoRuO$_6$, Phys. Rev. B **101**, 064419 (2020).

[28] J. W. G. Bos and J. P. Attfield, Magnetic frustration in La(A)CoNbO$_6$ (A = Ca, Sr, and Ba) double perovskites, Phys. Rev. B **70**, 174434 (2004).

[29] A. Kumar, R. Shukla, A. Pandey, S. Dalal, M. Miryala, K. Ueno, M. Murakami, and R. S. Dhaka, Structural, transport, optical, and electronic properties of Sr$_2$CoNbO$_6$ thin films, J. Appl. Phys. **128**, 025303 (2020).

[30] A. Kumar, R. Meena, M. Miryala, K. Ueno, and R. S. Dhaka, Effect of the growth orientation on the physical properties of Sr$_2$CoNbO$_6$ thin films, J. Vac. Sci. Technol. A **41**, 053409 (2023).

[31] L. T. Coutrim, E. M. Bittar, F. Garcia, and L. Bufaiçal, Influence of spin glass-like magnetic relaxation on the zero-field-cooled exchange bias effect, Phys. Rev. B **98**, 064426 (2018).

[32] L. T. Coutrim, D. Rigitano, C. Macchiutti, T. J. A. Mori, R. Lora-Serrano, E. Granado, E. Sadrollahi, F. J. Litterst, M. B. Fontes, E. Baggio-Saitovich, E. M. Bittar, and L. Bufaiçal, Zero-field-cooled exchange bias effect in phase-segregated La$_{2-x}$A$_x$CoMnO$_{6-\delta}$ (A = Ba, Ca, Sr; x = 0, 0.5), Phys. Rev. B **100**, 054428 (2019).

[33] R. Pradheesh, H. S. Nair, V. Sankaranarayanan, and K. Sethupathi, Exchange bias and memory effect in double perovskite Sr$_2$FeCoO$_6$, Appl. Phys. Lett. **101**, 142401 (2012).

[34] W. Liu, L. Shi, S. Zhou, J. Zhao, Y. Li, and Y. Guo, Griffiths phase, spin-phonon coupling, and exchange bias effect in double perovskite Pr$_2$CoMnO$_6$, J. Appl. Phys. **116**, 193901 (2014).

[35] L. T. Coutrim, E. M. Bittar, F. Stavale, F. Garcia, E. Baggio-Saitovich, M. Abbate, R. J. O. Mossanek, H. P. Martins, D. Tobia, P. G. Pagliuso, and L. Bufaiçal, Compensation temperatures and exchange bias in La$_{1.5}$Ca$_{0.5}$CoIrO$_6$, Phys. Rev. B **93**, 174406 (2016).

[36] J. K. Murthy, K. D. Chandrasekhar, H. C. Wu, H. D. Yang, J. Y. Lin, and A. Venimadhav, Antisite disorder driven spontaneous

exchange bias effect in $La_{2-x}Sr_xCoMnO_6 (0 \leqslant x \leqslant 1)$, J. Phys.: Condens. Matter **28**, 086003 (2016).

[37] A. Banerjee, J. Sannigrahi, S. Giri, and S. Majumdar, Magnetization reversal and inverse exchange bias phenomenon in the ferrimagnetic polycrystalline compound Er_2CoMnO_6, Phys. Rev. B **98**, 104414 (2018).

[38] M. T. Azcondo, J. R. de Paz, K. Boulahya, C. Ritter, F. García-Alvarado, and U. Amador, Complex magnetic behaviour of $Sr_2CoNb_{1-x}Ti_xO_6 (0 \leqslant x \leqslant 0.5)$ as a result of a flexible microstructure, Dalton Trans. **44**, 3801 (2015).

[39] R. D. Shannon, Revised effective ionic radii and systematic studies of interatomic distances in halides and chalcogenides, Acta Crystallogr. **32**, 751 (1976).

[40] A. Kumar, R. Shukla, R. Kumar, R. J. Choudhary, S. N. Jha, and R. S. Dhaka, Probing the electronic and local structure of $Sr_{2-x}La_xCoNbO_6$ using near-edge and extended x-ray absorption fine structures, Phys. Rev. B **105**, 245155 (2022).

[41] A. Kumar, B. Schwarz, H. Ehrenberg, and R. S. Dhaka, Evidence of discrete energy states and cluster-glass behavior in $Sr_{2-x}La_xCoNbO_6$, Phys. Rev. B **102**, 184414 (2020).

[42] A. Kumar, A. Jain, S. M. Yusuf, and R. S. Dhaka, Observation of anisotropic thermal expansion and the Jahn–Teller effect in double perovskites $Sr_{2-x}La_xCoNbO_6$ using neutron diffraction, J. Phys. Chem. Lett. **13**, 3023 (2022).

[43] K. Binder and A. P. Young, Spin glasses: Experimental facts, theoretical concepts, and open questions, Rev. Mod. Phys. **58**, 801 (1986).

[44] M. Gabay and G. Toulouse, Coexistence of spin-glass and ferromagnetic orderings, Phys. Rev. Lett. **47**, 201 (1981).

[45] D. M. Cragg, D. Sherrington, and M. Gabay, Instabilities of an m-vector spin-glass in a field, Phys. Rev. Lett. **49**, 158 (1982).

[46] D. M. Cragg and D. Sherrington, Spin-glass with local uniaxial anisotropy, Phys. Rev. Lett. **49**, 1190 (1982).

[47] P. Bag, P. R. Baral, and R. Nath, Cluster spin-glass behavior and memory effect in $Cr_{0.5}Fe_{0.5}Ga$, Phys. Rev. B **98**, 144436 (2018).

[48] P. M. Shand, T. Rash, M. Streicher, T. E. Kidd, K. R. Boyle, and L. H. Strauss, Coercivity and exchange bias of $Mn_{0.25}Ti_{1.1}S_2$ in the cluster-glass state, Phys. Rev. B **82**, 214413 (2010).

[49] S. Wakimoto, S. Ueki, Y. Endoh, and K. Yamada, Systematic study of short-range antiferromagnetic order and the spin-glass state in lightly doped $La_{2-x}Sr_xCuO_4$, Phys. Rev. B **62**, 3547 (2000).

[50] A. Senchuk, H. P. Kunkel, R. M. Roshkoa, C. Viddal, Li Wei, G. Williams, and X. Z. Zhou, $La_{0.5}Sr_{0.5}CoO_3$: A ferromagnet with strong irreversibility, Eur. Phys. J. B **37**, 285 (2004).

[51] A. P. Malozemoff, S. E. Barnes, and B. Barbara, Non-mean-field interpretation of the irreversibility line in spin-glasses, Phys. Rev. Lett. **51**, 1704 (1983).

[52] S. N. Kaul and S. Srinath, Irreversibility lines in the H–T phase diagram of re-entrant amorphous ferromagnets, J. Phys.: Condens. Matter **10**, 11067 (1998).

[53] J. R. L. de Almeida and D. J. Thouless, Stability of the Sherrington-Kirkpatrick solution of a spin glass model, J. Phys. A: Math. Gen. **11**, 983 (1978).

[54] G. Kotliar and H. Sompolinsky, Phase transition in a Dzyaloshinsky-Moriya spin-glass, Phys. Rev. Lett. **53**, 1751 (1984).

[55] M. R. Chowdhury, M. S. Seehra, P. Pramanik, S. Ghosh, T. Sarkar, B. Weise, and S. Thota, Antiferromagnetic short-range

order and cluster spin-glass state in diluted spinel $ZnTiCoO_4$, J. Phys.: Condens. Matter **34**, 275803 (2022).

[56] S. Chakravarty, O. S. Fjellvåg, A. Bhattacharyya, L. Keller, and S. Nair, Disorder-driven cluster glass state in a geometrically frustrated hexagonal perovskite, Phys. Rev. B **107**, 134414 (2023).

[57] S. V. Andreev, M. I. Bartashevich, V. I. Pushkarsky, V. N. Maltsev, L. A. Pamyatnykh, E. N. Tarasov, N. V. Kudrevatykh, and T. Goto, Law of approach to saturation in highly anisotropic ferromagnets application to Nd Fe B melt-spun ribbons, J. Alloys Compd. **260**, 196 (1997).

[58] F. E. Mabbs and D. J. Machin, *Magnetism and Transition Metal Complexes* (Chapman and Hall, London, 1973).

[59] F. Lloret, M. Julve, J. Cano, R. Ruiz-García, and E. Pardo, Magnetic properties of six-coordinated high-spin Co(II) complexes: Theoretical background and its application, Inorg. Chim. Acta **361**, 3432 (2008).

[60] M. C. Viola, M. J. Martínez-Lope, J. A. Alonso, J. L. Martínez, J. M. D. Paoli, S. Pagola, J. C. Pedregosa, M. T. FernándezDíaz, and R. E. Carbonio, Structure and magnetic properties of Sr_2CoWO_6: An ordered double perovskite containing Co^{2+}(HS) with unquenched orbital magnetic moment, Chem. Mater. **15**, 1655 (2003).

[61] S. Banerjee, D. P. Panda, P. Yanda, and A. Sundaresan, Canonical spin glass and cluster glass behavior in the polymorphs of $LiFeSnO_4$, Phys. Rev. Mater. **7**, 034405 (2023).

[62] R. Kumar, P. Yanda, and A. Sundaresan, Cluster-glass behavior in the two-dimensional triangular lattice Ising-spin compound $Li_2Mn_3O_7$, Phys. Rev. B **103**, 214427 (2021).

[63] J. Nogués, J. Sort, V. Langlais, V. Skumryev, S. Suriñach, J. S. Muñoz, and M. D. Baró, Exchange bias in nanostructures, Phys. Rep. **422**, 65 (2005).

[64] X. K. Zhang, J. J. Yuan, Y. M. Xie, Y. Yu, F. G. Kuang, H. J. Yu, X. R. Zhu, and H. Shen, Phase coexistence and exchange-bias effect in $LiMn_2O_4$ nanorods, Phys. Rev. B **97**, 104405 (2018).

[65] R. R. Das, P. Parida, A. K. Bera, T. Chatterji, B. R. K. Nanda, and P. N. Santhosh, Giant exchange bias in the single-layered Ruddlesden-Popper perovskite $SrLaCo_{0.5}Mn_{0.5}O_4$, Phys. Rev. B **98**, 184417 (2018).

[66] F. Radu, M. Etzkorn, R. Siebrecht, T. Schmitte, K. Westerholt, and H. Zabel, Interfacial domain formation during magnetization reversal in exchange-biased CoO/Co bilayers, Phys. Rev. B **67**, 134409 (2003).

[67] Y. Tang, Y. Sun, and Z. Cheng, Exchange bias associated with phase separation in the perovskite cobaltite $La_{1-x}Sr_xCoO_3$, Phys. Rev. B **73**, 174419 (2006).

[68] D. Niebieskikwiat and M. B. Salamon, Intrinsic interface exchange coupling of ferromagnetic nanodomains in a charge ordered manganite, Phys. Rev. B **72**, 174422 (2005).

[69] J. Nogués, D. Lederman, T. J. Moran, and I. K. Schuller, Positive exchange bias in FeF_2-Fe bilayers, Phys. Rev. Lett. **76**, 4624 (1996).

[70] J. Nogués, C. Leighton, and I. K. Schuller, Correlation between antiferromagnetic interface coupling and positive exchange bias, Phys. Rev. B **61**, 1315 (2000).

[71] A. Sahoo, P. Padhan, and W. Prellier, Interfacial antiferromagnetic coupling and dual-exchange bias in tetragonal $SrRuO_3$-$PrMnO_3$ superlattices, ACS Appl. Mater. Interfaces **9**, 36423 (2017).

[72] F. Hong, Z. Cheng, J. Wang, X. Wang, and S. Dou, Positive and negative exchange bias effects in the simple perovskite manganite $NdMnO_3$, Appl. Phys. Lett. **101**, 102411 (2012).

[73] J. Keller, P. Miltényi, B. Beschoten, G. Güntherodt, U. Nowak, and K. D. Usadel, Domain state model for exchange bias. II. Experiments, Phys. Rev. B **66**, 014431 (2002).

[74] P. V. M. Shameem and M. S. Kumar, Training effect of the exchange bias in sputter deposited Fe_3O_4 thin films with varying thickness, J. Magn. Magn. Mater. **458**, 241 (2018).

[75] L. Wee, R. L. Stamps, L. Malkinski, Z. Celinski, and D. Skrzypek, Thermal training of exchange bias in epitaxial $Fe/KNiF_3$, Phys. Rev. B **69**, 134425 (2004).

[76] D. Paccard, C. Schlenker, O. Massenet, R. Montmory, and A. Yelon, A new property of ferromagnetic-antiferromagnetic coupling, Phys. Status Solidi B **16**, 301 (1966).

[77] L. E. Fernandez-Outon, G. Vallejo-Fernandez, S. Manzoor, and K. O'Grady, Thermal instabilities in exchange biased materials, J. Magn. Magn. Mater. **303**, 296 (2006).

[78] C. Binek, Training of the exchange-bias effect: A simple analytic approach, Phys. Rev. B **70**, 014421 (2004).

[79] S. K. Mishra, F. Radu, H. A. Dürr, and W. Eberhardt, Training-induced positive exchange bias in NiFe/IrMn bilayers, Phys. Rev. Lett. **102**, 177208 (2009).

[80] J. Ventura, J. P. Araujo, J. B. Sousa, A. Veloso, and P. P. Freitas, Training effect in specular spin valves, Phys. Rev. B **77**, 184404 (2008).

[81] J. B. Goodenough, Theory of the role of covalence in the perovskite-type manganites [La, M (II)]MnO_3, Phys. Rev. **100**, 564 (1955).

[82] J. Kanamori, Superexchange interaction and symmetry properties of electron orbitals, J. Phys. Chem. Solids **10**, 87 (1959).